Guiding Electromagnetic Waves around Sharp Corners: Topologically Protected Photonic Transport in Metawaveguides

Tzuhsuan Ma,[1] Alexander B. Khanikaev,[3,4] S. Hossein Mousavi,[2] and Gennady Shvets[1,*]
[1]Department of Physics, The University of Texas at Austin, Austin, Texas 78712, USA
[2]Department of Electrical Engineering, The University of Texas at Austin, Austin, Texas 78712, USA
[3]Department of Physics, Queens College of The City University of New York, Queens, New York 11367, USA
[4]The Graduate Center of The City University of New York, New York, New York 10016, USA
(Received 6 November 2014; published 23 March 2015)

The wave nature of radiation prevents its reflections-free propagation around sharp corners. We demonstrate that a simple photonic structure based on a periodic array of metallic cylinders attached to one of the two confining metal plates can emulate spin-orbit interaction through bianisotropy. Such a metawaveguide behaves as a photonic topological insulator with complete topological band gap. An interface between two such structures with opposite signs of the bianisotropy supports topologically protected surface waves, which can be guided without reflections along sharp bends of the interface.

DOI: 10.1103/PhysRevLett.114.127401 PACS numbers: 78.67.Pt, 42.70.Qs, 73.20.Mf, 84.40.Az

Science thrives on analogies, and a considerable number of inventions and discoveries have been made by pursuing an unexpected connection to a very different field of inquiry. For example, photonic crystals (PhCs) have been referred to as "semiconductors of light" [1,2] because of the far-reaching analogies between electron propagation in a crystal lattice and light propagation in a periodically modulated photonic environment. However, one aspect of electron behavior, its *spin*, escaped emulation by photonic systems until the recent [3–7] invention of photonic topological insulators (PTIs). The impetus for these developments in photonics came from the discovery of topologically nontrivial phases in condensed-matter physics [8–13] that give rise to topologically protected edge states immune to scattering. The realization of topologically protected transport in simple PhCs would circumvent a fundamental limitation imposed by the wave equation: the inability of reflections-free light propagation along a sharply bent pathway. Topologically protected electromagnetic states could be used for transporting photons without any scattering, potentially underpinning new revolutionary concepts in applied science and engineering.

Several approaches to making PTIs have been explored across the electromagnetic spectrum, including magnetic photonic crystals [14–18], cavity arrays [3], coupled ring resonators [4,19], bianisotropic metamaterials [5], synthetic magnetic fields [6], and coupled helical fibers [7]. These approaches can be broadly separated into two groups: (a) those that rely on breaking the time-reversal symmetry (TRS) [6,14–18] and (b) those that do not violate the TRS [4,5]. We refer to the latter group of PTIs, which emulate the quantum spin Hall (SH) effect [9–13] and do not require an external magnetic field, as SH-PTIs. It was shown [5] that wave propagation in bianisotropic spin-degenerate metamaterials arranged into hexagonal PhCs can be described using the effective Kane-Mele Hamiltonian (KMH) introduced earlier [20,21] to model graphenelike topological insulators with strong spin-orbit coupling (SOC). The macroscopic size [4,19] and considerable complexity [5] of the proposed SH-PTIs rules them out as promising platforms for bending light on a wavelength spatial scale. One such greatly simplified photonic platform shown in Fig. 1(a) is proposed in this Letter: a bianisotropic metawaveguide (BMW) designed for emulating the KMH and providing photonic topological insulation.

The BMW is composed of the parallel-plate metal waveguide filled with a periodically arranged hexagonal array of metallic cylinders connected to the top and/or bottom metal plates located at $z = \pm h_0/2$. The finite bianisotropy [22] is generated by a finite vacuum gap ($g_1 \neq 0$) between the rods and one of the metal plates as illustrated in Fig. 1(c). The metal is modeled as a perfect electric conductor; i.e., the tangential component of the electric field vanishes at the metallic surface. In the analytically tractable case of $g_1 = 0$, the two (potentially degenerate) decoupled modes of interest of such a PhC waveguide can be classified as TM (with nonvanishing field components E_z, H_x, and H_y) and TE (with nonvanishing E_x, E_y, H_x, H_y, and H_z) modes [23]. Under the Bloch ansatz, the following field decomposition is assumed by retaining just two lowest-order transverse modes:

$$H_z^{\mathrm{TE}}(\boldsymbol{r},t) = \sum_{n,\boldsymbol{k}_\perp} a_e^n(\boldsymbol{k}_\perp) h_z^{n,\boldsymbol{k}_\perp}(\boldsymbol{r}_\perp) \cos\left(\frac{\pi}{h_0} z\right) e^{i\boldsymbol{k}_\perp\cdot\boldsymbol{r}_\perp - i\omega_n(\boldsymbol{k}_\perp)t} + \text{c.c.}, \tag{1}$$

$$E_z^{\mathrm{TM}}(\boldsymbol{r},t) = \sum_{n,\boldsymbol{k}_\perp} a_m^n(\boldsymbol{k}_\perp) e_z^{n,\boldsymbol{k}_\perp}(\boldsymbol{r}_\perp) e^{i\boldsymbol{k}_\perp\cdot\boldsymbol{r}_\perp - i\omega_n(\boldsymbol{k}_\perp)t} + \text{c.c.}, \tag{2}$$

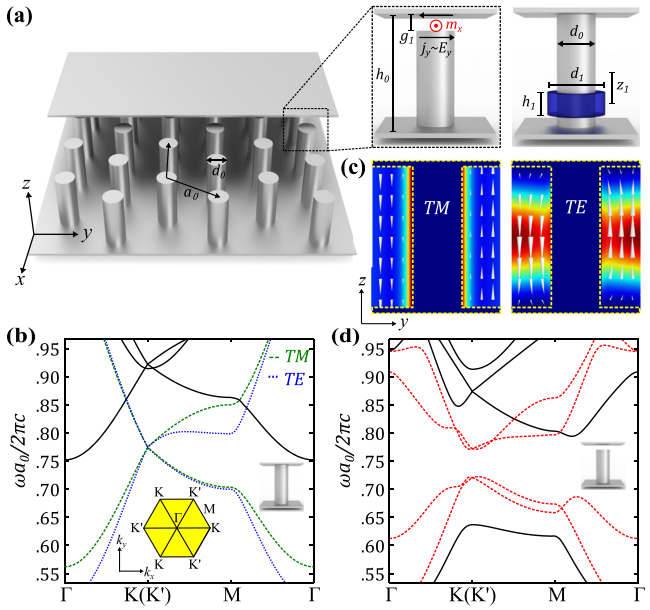

FIG. 1 (color online). BMW as a photonic topological insulator. (a) Schematic of the BMW. Part of the top metal plate is removed to reveal the "bed-of-nails" structure below. The enlarged regions on the right illustrate the origin of the bianisotropic response. Right inset: an equivalent way to produce bianisotropy by adding an asymmetrically placed metallic volume (washer) around the rod. (b) PBS of spin-degenerate metawaveguide ($g_1 = 0$) with TE and TM modes forming doubly degenerate Dirac cones at $K(K')$ points. (c) Field profiles of the degenerate TE and TM mode at the K point. Colors: energy density. Arrows: electric field for the TM mode and magnetic field for the TE mode. Yellow dashed line: metallic border. (d) PBS with the band gap induced by the bianisotropy of the metawaveguide ($g_1 = g_0$). Dashed lines in (b) and (d): TE and TM bands of interest. BMW parameters: $h_0 = a_0$, $d_0 = 0.345a_0$, $g_0 = 0.15a_0$.

where $\boldsymbol{r}_\perp = (x, y)$, $\boldsymbol{k}_\perp = (k_x, k_y)$ are the Bloch wave numbers inside the Brillouin zone (BZ), $h_z^{n,\boldsymbol{k}_\perp}(\boldsymbol{r}_\perp)$ and $e_z^{n,\boldsymbol{k}_\perp}(\boldsymbol{r}_\perp)$ are the normalized periodic field profiles such that $\int_{\text{cell}} dV(\epsilon|\boldsymbol{e}^{n,\boldsymbol{k}_\perp}|^2 + \mu_0|\boldsymbol{h}^{n,\boldsymbol{k}_\perp}|^2) = 1$, and the $n = -, +$ index refers to lower (upper) propagation bands. Note that in limiting the expansion basis and thereby constraining the z dependence of the fields, the above ansatz is a crucial simplification that is needed to make further analytic progress. However, all numerical results shown in Figs. 1–4 are obtained using first-principles electromagnetic simulations of COMSOL Multiphysics that are not subject to the reduced expansion basis approximation given by Eqs. (1) and (2).

The eigenfrequencies $\omega_n(\boldsymbol{k}_\perp)$ are doubly degenerate for $\boldsymbol{k}_\perp = \pm\boldsymbol{e}_x 4\pi/3a_0$ corresponding to the $K(K')$ edges of the Brillouin zone shown in the inset to Fig. 1(b). The hexagonal symmetry of the "photonic graphene" [24] lattice guarantees the appearance of the Dirac cone for the decoupled TE and TM modes. The field profiles of the two degenerate modes are shown in Fig. 1(c). The photonic band structure plotted in Fig. 1(b) shows the degenerate TE and TM Dirac cones overlapping at the K point of the Brillouin zone at the frequency $\omega_D = \omega_D^{\text{TE}} = \omega_D^{\text{TM}}$. For a given period a_0, the degeneracy between TE and TM modes' frequencies and group velocities $v_D \equiv \partial\omega/\partial k$ is obtained by the judicious choice of h_0 and the cylinders' diameter d_0. Such mode degeneracy is essential [5] for establishing spinlike linear combinations of the TE and TM modes that can be coupled to each other by a bianisotropic perturbation of the photonic structure.

Opening an air gap breaks the σ_z mirror symmetry and introduces the requisite bianisotropic response of the metawaveguide [22] as schematically explained in Fig. 1(a), right insets: the electric field in the gap between the cylinder and the plate $E_{x(y)}$ induces antisymmetric currents $j_{x(y)}$ producing the net orthogonal magnetic moment $m_{y(x)}$ and vice versa. The photonic band structure (PBS) of the resulting bianisotropic crystal ($g_1 = g_0 \equiv 0.15a_0$) is shown in Fig. 1(d), indicating that a complete photonic band gap is formed in the $0.72 < \omega a_0/2\pi c < 0.77$ frequency range. As analytically demonstrated below, the finite rod-plate gap mimics the SOC in a graphenelike photonic structure, thereby turning the BMW shown in Fig. 1 into a PTI as long as the lowest-order TE and TM modes are dominant.

The effective Hamiltonian for the photonic states of the BMW in the vicinity of the K point is constructed by combining two methodologies: (a) degenerate perturbation theory originally developed [15] for nonreciprocal photonic crystals supporting a doubly degenerate TM mode and (b) the classic Slater theory [25] describing the modification of the modes of an electromagnetic cavity by the perturbation of its boundaries (see the Supplemental Material for detailed derivations [26]). These two techniques are applied to a BMW perturbed by an asymmetric addition of a metal volume ("washer") shown in the Fig. 1(a) right inset, which is conceptually equivalent to the asymmetric gap as far as its bianisotropic response is concerned. The unperturbed basis for the perturbation theory at the K point consists of the TE and TM modes whose field profiles are shown in Fig. 2. The modes' dispersion relations $\omega_\pm(\delta\boldsymbol{k}) = \omega_{e,m} \pm v_D|\delta\boldsymbol{k}|$ are linear [15] in $\delta\boldsymbol{k} \equiv \boldsymbol{k} - \boldsymbol{K}$ in the vicinity of the Dirac point, at which the frequencies of the TE and TM modes are $\omega_{e,m}$, respectively.

Finite $\delta\boldsymbol{k} \neq \boldsymbol{0}$ breaks the degeneracy for each mode and, for $\delta k > 0$, renders the upper (lower) band modes forward (backward) propagating as shown in Fig. 2. We also observe that the basis eigenmodes become linearly polarized (LP) based on the average direction of their magnetic field: the forward (backward) modes $e_+(m_-)$ are x polarized while the backward (forward) modes $e_-(m_+)$ are y polarized. The boundary perturbation couples the ith and jth basis modes with the normalized coupling coefficient given by $\Delta_{ij} = -\int_{\Delta V}(\boldsymbol{e}_i^* \cdot \boldsymbol{e}_j - \boldsymbol{h}_i^* \cdot \boldsymbol{h}_j)dV$, where ΔV is the volume displaced by the metal washer. Using a

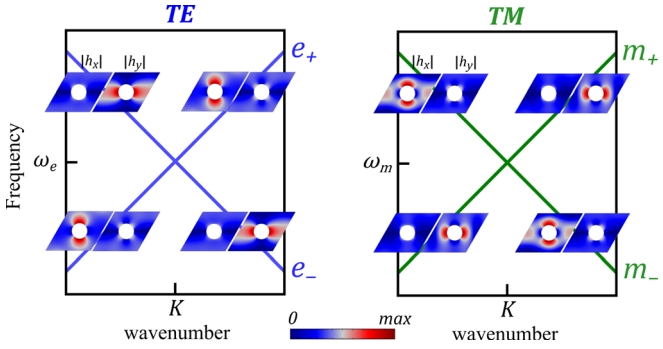

FIG. 2 (color online). Dirac dispersion of the dipolar TE and dipolar TM modes in the vicinity of the K point. The in-plane magnetic field profiles ($|h_x|$ on the left and $|h_y|$ on the right) are overlaid atop the band structure to show the dominant component of the magnetic field. The positive- and negative-group-velocity bands are labeled with "+" and "−" signs.

vector representation $\boldsymbol{a}_e = [a_{e_-}; a_{e_+}]$ and $\boldsymbol{a}_m = [a_{m_-}; a_{m_+}]$ [where $a_{e(m)\pm}$ is shorthand for $a^{\pm}_{e(m)}(\boldsymbol{K}+\delta\boldsymbol{k})$] for the complex-valued amplitudes of the expansion basis, we calculate the perturbed frequencies $\omega'(\delta\boldsymbol{k})$ by solving the following eigenvalue equation:

$$\begin{bmatrix} \omega_e(1+\Delta_{ee})\hat{I} - v_D|\delta\boldsymbol{k}|\hat{\sigma}_z & -\omega_e\Delta_{em}\hat{\sigma}_y \\ -\omega_m\Delta_{em}\hat{\sigma}_y & \omega_m(1+\Delta_{mm})\hat{I} - v_D|\delta\boldsymbol{k}|\hat{\sigma}_z \end{bmatrix} \times \begin{bmatrix} \boldsymbol{a}_e \\ \boldsymbol{a}_m \end{bmatrix} = \omega' \begin{bmatrix} \boldsymbol{a}_e \\ \boldsymbol{a}_m \end{bmatrix}, \tag{3}$$

where $\hat{\sigma}_x, \hat{\sigma}_y, \hat{\sigma}_z$ are the Pauli matrices, and $\hat{I}$ is a 2×2 unity matrix.

According to Eq. (3), the perturbation has two effects on the modes. First, the modes' frequencies $\omega_{e,m}$ are renormalized by the diagonal Δ_{ee}/Δ_{mm} terms. Second, the cross-coupling bianisotropic terms $\Delta_{em}(d_1, h_1; z_1) = \int_{\Delta V} \boldsymbol{h}_e^* \cdot \boldsymbol{h}_m dV = -\Delta_{em}(d_1, h_1; -z_1)$ satisfy the following selection rule that follows from the field profiles shown in Fig. 2: they couple the TE and TM modes propagating in the opposite directions. The antisymmetry of Δ_{em} with respect to z_1 follows from the eigenmodes' symmetry: $h_{e,x/y}(x,y,-z) = -h_{e,x/y}(x,y,z)$ and $h_{m,x/y}(x,y,-z) = +h_{m,x/y}(x,y,z)$.

The effective Hamiltonian $\mathscr{H}^{em}_K$ represented by the 4×4 matrix in the lhs of Eq. (3) can be transformed to $\mathscr{H}^{\uparrow\downarrow}_K = U\mathscr{H}^{em}_K U^{-1}$ by a unitary transformation from the LP basis $\mathbf{A}_K = [\boldsymbol{a}_e; \boldsymbol{a}_m]$ of the TE and TM modes to a circularly polarized (CP) basis $\boldsymbol{\Psi}_K = U\mathbf{A}_K$ of spin states, where the transformation matrix U is given by the following Kronecker product:

$$U = \frac{1}{2}\begin{pmatrix} 1-\beta & 1+\beta \\ 1-\beta & -1-\beta \end{pmatrix} \otimes \begin{pmatrix} e^{-i\phi/2} & ie^{-i\phi/2} \\ -e^{i\phi/2} & ie^{i\phi/2} \end{pmatrix}, \tag{4}$$

where $2\omega_D = \omega_e + \omega_m$, $2\Delta\omega_D = \omega_e - \omega_m$, $2\omega'_D = \omega_e(1+\Delta_{ee}) + \omega_m(1+\Delta_{mm})$, $2\Delta\omega'_D = \omega_e(1+\Delta_{ee}) - \omega_m(1+\Delta_{mm})$, and $\beta = \Delta\omega_D/2\omega_D$ and the phase ϕ is defined by $|\delta\boldsymbol{k}|e^{i\phi} \equiv \delta k_x + i\delta k_y$. It is possible to design the "dressed" frequencies $\omega'_e = \omega_e(1+\Delta_{ee})$ and $\omega'_m = \omega_m(1+\Delta_{mm})$ to be equal to each other, in which case the spin-degeneracy [5] condition $\Delta\omega'_D = 0$ is satisfied. The resulting eigenvalue equation $\mathscr{H}^{\uparrow\downarrow}_K \boldsymbol{\Psi}_K = \Omega\boldsymbol{\Psi}_K$ then assumes a block-diagonal form

$$\begin{bmatrix} v_D\delta\boldsymbol{k}\cdot\boldsymbol{\sigma} + \omega_D\Delta_{em}\hat{\sigma}_z & 0 \\ 0 & v_D\delta\boldsymbol{k}\cdot\boldsymbol{\sigma} - \omega_D\Delta_{em}\hat{\sigma}_z \end{bmatrix} \begin{bmatrix} \boldsymbol{\psi}^{\uparrow}_K \\ \boldsymbol{\psi}^{\downarrow}_K \end{bmatrix} = \Omega \begin{bmatrix} \boldsymbol{\psi}^{\uparrow}_K \\ \boldsymbol{\psi}^{\downarrow}_K \end{bmatrix} \tag{5}$$

where $\boldsymbol{\sigma} = (\hat{\sigma}_x, \hat{\sigma}_y)$, and $\boldsymbol{\psi}^{\uparrow(\downarrow)}_K \equiv [\psi^{R,\uparrow(\downarrow)}_K; \psi^{L,\uparrow(\downarrow)}_K]$ are the spin-up (-down) components of the $\boldsymbol{\Psi}_K \equiv [\boldsymbol{\psi}^{\uparrow}_K; \boldsymbol{\psi}^{\downarrow}_K]$ eigenvector, and $\Omega = \omega' - \omega'_D$ is the detuning from the dressed Dirac frequency ω'_D.

The physical meaning of the new spin-polarized CP photonic states ("R" for right and "L" for left) is clarified by calculating $U^{-1}\boldsymbol{\Psi}_K$ to obtain the following expressions in the original TE and TM LP basis under the $\beta \ll 1$ assumption: $\boldsymbol{\Psi}^{R/L,\uparrow}_K = [1; \mp i; 1; \mp i]$ and $\boldsymbol{\Psi}^{R/L,\downarrow}_K = [1; \mp i; -1; \pm i]$. Therefore, the relative phase between TE and TM modes represents [5] the spin degree of freedom (DOF), and the handedness (i.e., the phase shift between the two LP components) represents the orbital DOF. By introducing Pauli matrices $\hat{s}$ that act on the spin components of $\boldsymbol{\Psi}_K$, Eq. (5) can be written in a more compact form as $\mathscr{H}^{\uparrow\downarrow}_K = v_D\hat{s}_0(\delta k_x\hat{\sigma}_x + \delta k_y\hat{\sigma}_y) + \omega_D\Delta_{em}\hat{s}_z\hat{\sigma}_z$, where $\hat{s}_0$ is a unity matrix, and the Kronecker product shorthand (e.g., $\hat{s}_0\hat{\sigma}_z \equiv \hat{s}_0 \otimes \hat{\sigma}_z$) is used.

Expanding the space of photonic states to include the vicinities of both K and K' points, i.e., by introducing the 8-component spinor $\boldsymbol{\Psi} = [\boldsymbol{\Psi}_K; \boldsymbol{\Psi}_{K'}]$, the combined 8×8 effective Hamiltonian matrix can be written (see the Supplemental Material [26]) as

$$\mathscr{H} = v_D(\delta k_x\hat{\tau}_z\hat{s}_0\hat{\sigma}_x + \delta k_y\hat{\tau}_0\hat{s}_0\hat{\sigma}_y) + \omega_D\Delta_{em}\hat{\tau}_z\hat{s}_z\hat{\sigma}_z, \tag{6}$$

where $\hat{\tau}_z$ and $\hat{\tau}_0$ are the Pauli and identity matrices acting on the subspace combining the K and K' points of the BZ. Because Eq. (6) is identical to KMH [20], it defines the photonic modes that have the same topological nature as the electronic states in graphene with strong SOC described by the last term. Therefore, the BMW is an example of a SH-PTI that possesses a spectral band gap $\Delta\omega_{\text{gap}} = 2\omega_D|\Delta_{em}|$ induced by the bianisotropy. An interface between two BMWs with opposite signs of Δ_{em} exemplified in Fig. 3(a) is, therefore, expected to support two pairs [5,14] of topologically protected surface waves (TPSWs). This prediction is confirmed using first-principles COMSOL

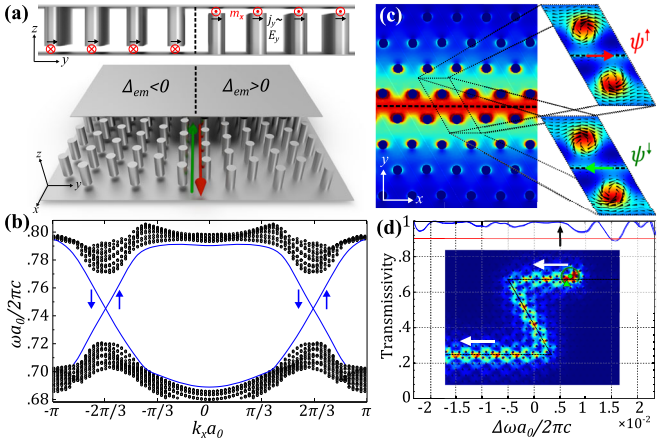

FIG. 3 (color online). Propagation of TPSWs along the interface between two topologically nontrivial BMWs (a) Side and top views of the topologically nontrivial interface (dashed line) between two BMWs introduced in Fig. 1. (b) 1D PBS of a supercell (single cell along the x direction, 30 cells on each side of the interface) of the hybridized TE and TM modes. Black circles: bulk modes, blue lines: TPSW, arrows: spin state. (c) Color: energy density; arrows: Poynting flux of a TPSW at the frequency ω indicated by a black arrow in (d). (d) Transmission spectrum $T(\Delta\omega)$ through the zigzag path, where $\Delta\omega = \omega - \omega_G$ is the detuning from the band gap center at $\omega_G a_0/2\pi c = 0.745$. Spin-down TPSWs are excited by placing an L-polarized electric dipole between the rod and metal plate in the upper right corner. Red line:$T = 0.9$; BMW parameters: same as in Fig. 1.

simulations of the PBS of the double-BMW plotted Fig. 3(b), where four spin-locked surface photonic modes (one forward-propagating spin-up pair and another backward-propagating spin-down pair) are plotted with solid lines.

Several important properties of TPSWs can be observed from Fig. 3. First, these are indeed surface modes because their energy density is tightly confined to the topological interface as shown in Fig. 3(c). Second, the polarization state of TPSWs is spatially entangled [5] with the spin state. Specifically, from the directional flow of the Poynting flux plotted with arrows in Fig. 3(c) inside the rod-plate gap, we observe that the spin-up and spin-down surface modes have opposite handedness: $R\,(L)$ for the spin-up (spin-down) states. This essential feature enables directional excitation of TPSWs with a single rotating electric or magnetic dipole. By placing an L-polarized dipole inside the air gap adjacent to the interface, backward-propagating spin-down TPSW is excited as shown in Fig. 3(d). In contrast, directional excitation of topologically trivial surface waves requires a series of phase-shifted dipoles placed along the propagation directions [26], thereby increasing the device size.

Third, the gapless crossing of the surface modes corresponding to the different spin states shown in Fig. 3(b) indicates the lack of spin flipping. The spin conservation results in a topologically protected spin-polarized transport of TPSWs: their backscattering is expected to be suppressed even in the presence of various classes of structural perturbations (e.g., the variation of the gap size g_1 or gap position $z_1 = \pm h_0/2$) that preserve spin degeneracy. Below, we concentrate on a specific type of imperfection: a sharp bend of the interface shown in Fig. 3(d). Because spin degeneracy is maintained by such imperfections, we can expect that it should be possible to direct the flow of TPSWs along the bend without reflections. The results of a COMSOL simulation are shown in Fig. 3(d), where we have investigated the transmission of a spin-polarized TPSW launched from the upper-right corner of a zigzag interface between two BMWs with opposite bianisotropy coefficients Δ_{em}. High broadband transmission of TPSWs, such that $T(\omega) > 0.9$ is achieved for 98% of the entire band gap, is observed, indicating that two 120° turns of the wave along the correspondingly bent topological interface are accomplished with negligible reflection. Although the demonstrated topological protection is conceptually understood from our analytic theory that relies on the limited basis expansion given by Eqs. (1) and (2), the actual results shown in Fig. 3 are obtained using first-principles electromagnetic simulations.

The unusual nature of such reflection-free propagation of an electromagnetic wave along a sharply curved interface can be appreciated by comparing it with the case of a standard (topologically trivial) interface between two photonic crystals with overlapping photonic band gaps. We make such a comparison by considering an interface between two topologically trivial PhCs shown in Fig. 4(a). Each PhC consists of a hexagonal array of identical semicircular metal rods attached to two metallic plates for vertical confinement. The interface between these PhCs is introduced by changing the orientation of the rods. The two PhCs possess identical gapped spectra shown in Fig. 4(b). Different surface terminations of the PhCs form an interface supporting topologically trivial surface waves (TTSWs) [33] inside the band gap. The propagation band $\omega_{\mathrm{TM}}^{\mathrm{TTSW}}(k_x)$ of the TTSW shown by the blue lines in Fig. 4(b) was numerically calculated for the TM polarization. Any wavelength-scale perturbation of the interface (e.g., change in the rod's size or orientation), including a sharp bending of the interface, can induce reflections by scattering the forward-moving TTSW into its backward-moving counterpart.

One such zigzag propagation path corresponding to two 120° bends of the domain wall is shown in Fig. 4(c). The transmission $T(\omega)$ of a TTSW launched by a point dipole placed in the upper-right corner of the simulation domain was numerically calculated for a range of frequencies spanning the entire band gap of the interface-forming PhCs. The plot of $T(\omega)$ in Fig. 4(d) exhibits two sharp 100% transmission peaks within the band gap region. These transmission peaks are related to the phenomenon

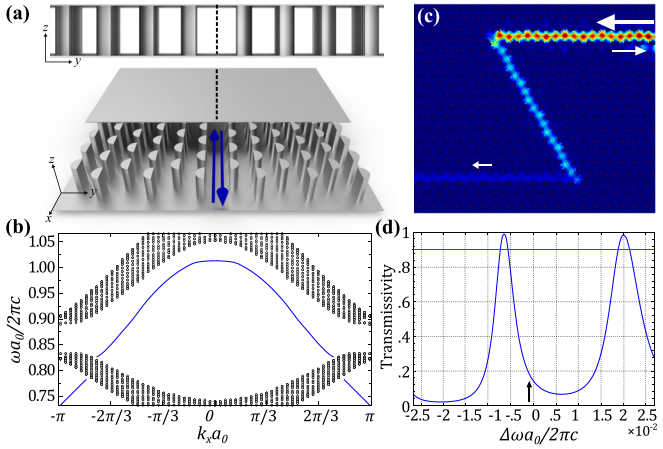

FIG. 4 (color online). Propagation of surface waves along the interface between two topologically trivial PhCs. (a) Side and top views of the two PhCs and their interface. Semicircular metal rods arranged in a hexagonal pattern connect the two metal plates. (b) 1D PBS of a supercell (a single unit cell along the x axis, 30 unit cells on each side of the interface along y axis) for TM modes. Black circles: bulk modes, blue lines: TTSWs. (c) Energy density of a TTSW with frequency indicated by the black arrow in (d). (d) Transmission spectrum $T(\omega)$ through the zigzag route, where ω spans the entire band gap and $\Delta\omega = 0$ corresponds to band gap center at $\omega a_0/2\pi c = 0.86$. Red line: $T = 0.9$. Structure parameters: $h_0 = a_0$, $d = 0.6a_0$.

of resonant tunneling [34,35] through the cavity formed by the middle portion ("cavity") of the zigzag. Their spectral positions, often referred to as Fabry-Perot resonances, are determined by the length of the cavity. Backscattering is essential for the formation of Fabry-Perot resonances because, at peak transmission, TTSWs undergo multiple bounces inside the cavity. However, for all other frequencies inside the band gap the transmission is very small. According to Fig. 4(d), $T(\omega) > 0.9$ is achieved for just 5.6% of the entire band gap. While it has been recently demonstrated [36] that it may be possible to reduce broadband wave reflections from PhC waveguides that are bent by as much as 90° by carefully designing the geometry of the bends, the general conclusion holds: complete elimination of reflections is only possible at Fabry-Perot resonances. This result should be contrasted with near-perfect transmission of TPSWs over the entire band gap through an identical sequence of two bends of the mode-guiding interface shown in Fig. 3(d).

In conclusion, a simple design of a topological photonic insulator emulating the Kane-Mele Hamiltonian with tunable spin-orbit interaction—a BMW—has been introduced. Unlike earlier metamaterials-based designs, BMWs are nonresonant photonic structures that do not suffer from high Ohmic losses and could be potentially scaled to infrared optical frequencies. Domain walls between BMWs with reversed bianisotropy coefficient support TPSWs that are formally described as photonic states with a conserved spinlike degree of freedom propagating in the direction prescribed by the sign of the spin. While the standard scalar wave equation in general prohibits reflectionless propagation of electromagnetic waves along the paths that are nonsmooth on the wavelength spatial scale, the multicomponent polarization state of TPSWs enables their guiding along sharply curved interfaces with negligible reflection as confirmed by our first-principles electromagnetic simulations. This unique functionality makes BMWs a promising platform for developing various applications in photonics and electromagnetics that benefit from compact and reflectionless routing of electromagnetic energy.

This work was supported by the National Science Foundation (NSF) Grants No. DMR-1120923 and No. PHY-1415547.

*gena@physics.utexas.edu

[1] E. Yablonovitch, Inhibited Spontaneous Emission in Solid-State Physics and Electronics, Phys. Rev. Lett. **58**, 2059 (1987).
[2] S. John, Strong Localization of Photons in Certain Disordered Dielectric Superlattices, Phys. Rev. Lett. **58**, 2486 (1987).
[3] R. Umucalılar and I. Carusotto, Artificial gauge field for photons in coupled cavity arrays, Phys. Rev. A **84**, 043804 (2011).
[4] M. Hafezi, E. A. Demler, M. D. Lukin, and J. M. Taylor, Robust optical delay lines with topological protection, Nat. Phys. **7**, 907 (2011).
[5] A. B. Khanikaev, S. H. Mousavi, W.-K. Tse, M. Kargarian, A. H. MacDonald, and G. Shvets, Photonic topological insulators, Nat. Mater. **12**, 233 (2013).
[6] K. Fang, Z. Yu, and S. Fan, Realizing effective magnetic field for photons by controlling the phase of dynamic modulation, Nat. Photonics **6**, 782 (2012).
[7] M. C. Rechtsman, J. M. Zeuner, Y. Plotnik, Y. Lumer, D. Podolsky, F. Dreisow, S. Nolte, M. Segev, and A. Szameit, Photonic Floquet topological insulators, Nature (London) **496**, 196 (2013).
[8] K. v. Klitzing, G. Dorda, and M. Pepper, New Method for High-Accuracy Determination of the Fine-Structure Constant based on Quantized Hall Resistance, Phys. Rev. Lett. **45**, 494 (1980).
[9] B. A. Bernevig, T. L. Hughes, and S.-C. Zhang, Quantum spin Hall effect and topological phase transition in HgTe quantum wells, Science **314**, 1757 (2006).
[10] M. Konig, S. Wiedmann, C. Brune, A. Roth, H. Buhmann, L. W. Molenkamp, X.-L. Qi, and S.-C. Zhang, Quantum spin Hall insulator state in HgTe quantum wells, Science **318**, 766 (2007).
[11] D. Hsieh, D. Qian, L. Wray, Y. Xia, Y. S. Hor, R. J. Cava, and M. Z. Hasan, A topological Dirac insulator in a quantum spin Hall phase, Nature (London) **452**, 970 (2008).
[12] Y. Xia *et al.*, Observation of a large-gap topological-insulator class with a single Dirac cone on the surface, Nat. Phys. **5**, 398 (2009).

[13] H. Zhang, C.-X. Liu, X.-L. Qi, X. Dai, Z. Fang, and S.-C. Zhang, Topological insulators in Bi_2Se_3, Bi_2Te_3 and Sb_2Te_3 with a single Dirac cone on the surface, Nat. Phys. **5**, 438 (2009).

[14] F. Haldane and S. Raghu, Possible Realization of Directional Optical Waveguides in Photonic Crystals with Broken Time-Reversal Symmetry, Phys. Rev. Lett. **100**, 013904 (2008).

[15] S. Raghu and F. D. M. Haldane, Analogs of quantum-hall-effect edge states in photonic crystals, Phys. Rev. A **78**, 033834 (2008).

[16] Z. Wang, Y. Chong, J. Joannopoulos, and M. Soljačić, Reflection-Free One-Way Edge Modes in a Gyromagnetic Photonic Crystal, Phys. Rev. Lett. **100**, 013905 (2008).

[17] Z. Wang, Y. Chong, J. D. Joannopoulos, and M. Soljačić, Observation of unidirectional backscattering-immune topological electromagnetic states, Nature (London) **461**, 772 (2009).

[18] Y. Poo, R. Wu, Z. Lin, Y. Yang, and C. T. Chan, Experimental Realization of Self-Guiding Unidirectional Electromagnetic Edge States, Phys. Rev. Lett. **106**, 093903 (2011).

[19] M. Hafezi, S. Mittal, J. Fan, A. Migdall, and J. M. Taylor, Imaging topological edge states in silicon photonics, Nat. Photonics **7**, 1001 (2013).

[20] C. L. Kane and E. J. Mele, Quantum Spin Hall Effect in Graphene, Phys. Rev. Lett. **95**, 226801 (2005).

[21] B. A. Bernevig and S.-C. Zhang, Quantum Spin Hall Effect, Phys. Rev. Lett. **96**, 106802 (2006).

[22] A. N. Serdyukov, I. V. Semchenko, S. A. Tretyakov, and A. Sihvola, *Electromagnetics of Bi-anisotropic Materials: Theory and Applications* (Gordon and Breach Science Publishers, Amsterdam, 2001).

[23] K. Sakoda, *Optical Properties of Photonic Crystals* (Springer, Berlin, 2001).

[24] A. Szameit, M. C. Rechtsman, O. Bahat-Treidel, and M. Segev, PT-symmetry in honeycomb photonic lattices, Phys. Rev. A **84**, 021806(R) (2011).

[25] J. C. Slater, Microwave electronics, Rev. Mod. Phys. **18**, 441 (1946).

[26] See the Supplemental Material at http://link.aps.org/supplemental/10.1103/PhysRevLett.114.127401, which includes Refs. [31–36], for details of analytic theory.

[27] C.-T. Tai, On the eigenfunction expansion of dyadic Green's functions. Proc. IEEE **61**, 480 (1973).

[28] R. E. Collin, I. Antennas, and P. Society, *Field Theory of Guided Waves* (IEEE Press, New York, 1991).

[29] R. S. Mong and V. Shivamoggi, Edge states and the bulk-boundary correspondence in Dirac Hamiltonians, Phys. Rev. B **83**, 125109 (2011).

[30] B. Simon, Holonomy, the Quantum Adiabatic Theorem, and Berry's Phase, Phys. Rev. Lett. **51**, 2167 (1983).

[31] D. Sheng, Z. Weng, L. Sheng, and F. Haldane, Quantum Spin-Hall effect and Topologically Invariant Chern Numbers, Phys. Rev. Lett. **97**, 036808 (2006).

[32] D. Thouless, M. Kohmoto, M. Nightingale, and M. Den Nijs, Quantized Hall Conductance in a Two-Dimensional Periodic Potential, Phys. Rev. Lett. **49**, 405 (1982).

[33] A. E. Krasnok, I. S. Maksymov, A. I. Denisyuk, P. A. Belov, A. E. Miroshnichenko, C. R. Simovski, and Yu. S. Kivshar, Optical nanoantennas. Phys. Usp. **56**, 539 (2013).

[34] R. D. Meade, K. D. Brommer, A. M. Rappe, and J. Joannopoulos, Electromagnetic Bloch waves at the surface of a photonic crystal, Phys. Rev. B **44**, 10961 (1991).

[35] S. Fan, P. R. Villeneuve, J. D. Joannopoulos, and H. Haus, Channel Drop Tunneling through Localized States, Phys. Rev. Lett. **80**, 960 (1998).

[36] A. Mekis, J. C. Chen, I. Kurland, S. Fan, P. R. Villeneuve, and J. D. Joannopoulos, High Transmission through Sharp Bends in Photonic Crystal Waveguides, Phys. Rev. Lett. **77**, 3787 (1996).